Fretting Characteristics of Textured TC4 Alloy Under Punch/Plane Contact: A Finite Element Study

Shenglin Liang, Xuanqi Sun, Dingjun She, Qingwen Dai, Wei Huang,* and Xiaolei Wang

Herein, the fretting behavior of textured surfaces with varying depths under punch/plane conditions for TC4 (Ti-6Al-4 V) is simulated using the finite element method . The effects of surface texture on mechanical properties, wear behavior, and fatigue characteristics are analyzed. The Archard and energy wear models are employed to simulate fretting behavior, while the Smith–Watson–Topper model is utilized to predict the fatigue damage. The interfacial dynamics remained unchanged in the presence of surface textures. Fretting states of the partial slip regime (PSR) or the gross slip regime (GSR) are identical under similar loading conditions for smooth as well as textured surfaces. In the PSR, the primary damage mechanism is fatigue cracking, and the fatigue life of textured surfaces decreased with increasing texture depth. Compared with the smooth sample, the fatigue life of the textured surface with 40 μm groove depth reduces by ≈6.3%. In the GSR, wear is observed to be the dominant damage mechanism, and textured surfaces demonstrated better anti-wear performance at lower displacement amplitudes (≤30 μm) when compared with the smooth surfaces.

1. Introduction

Fretting refers to the micro-amplitude relative slip at the interface of two closely fitted components, typically induced by vibration or other unbalanced external forces.[1,2] Fretting regimes are classified as stick regime , partial slip regime (PSR), and gross slip regime (GSR), which are based on the combination of normal load and displacement amplitude. In the SR, tangential displacement is minimal, resulting in minimal wear and higher fatigue life. The tangential displacement amplitude increases in the PSR, which primarily results in crack nucleation and propagation, and a reduced fatigue

life. In the GSR, tangential displacement is greater, and the rate of material removal surpasses the crack nucleation and propagation, causing severe wear. This phenomenon is widespread and experienced in several modern industries, including general machinery,[3,4] aerospace,[5–7] and railway.[8]

Titanium alloys, especially TC4 (Ti-6Al-4 V), are extensively used in the mechanical components of the naval and aerospace industries owing to their attractive mechanical properties, including a high strength-to-weight ratio and excellent corrosion resistance.[9,10] However, their service life is significantly compromised by fretting, particularly in dynamic load-bearing applications. Therefore, the damage mechanism and protection methods of titanium alloys against fretting have gained significant attention from researchers in both experimental and numerical simulation-based investigations. S. Fouvry et al.[9,11–13] conducted a series of investigations on fretting wear and crack initiation in TC4 alloy under various contact configurations, including sphere–plane, cylinder–plane, and punch–plane. The crack initiation rate in the contact area was observed to be inversely proportional to the wear rate. Hager et al.[14] conducted experimental investigations to characterize the critical normal load and displacement corresponding to the transition from PSR to GSR in the TC4/TC4 contact pair. A linear relationship between critical load and displacement was observed. Araujor et al.[15] conducted fretting fatigue tests under combined high-cycle fatigue and low-cycle fatigue loading regimes. The results indicated that fretting fatigue life is primarily influenced by the magnitude of the tangential force.

Numerical simulations have enabled researchers to investigate complicated engineering problems in a controlled environment, which can reduce both cost and time consumption. Several numerical simulation based investigations have been conducted to investigate the fretting fatigue phenomenon.[16–23] McColl et al.[16] proposed a modified version of Archard's equation method to simulate the fretting wear and evaluated the effect of the number of wear cycles in a cylinder-on-flat contact pair. Arnaud et al.[18] conducted a 2D finite element analysis (FEA) for TC4 with Smith–Watson–Topper (SWT) cumulative damage analysis to simulate crack nucleation domains under the PSR and the GSR. The results showed good agreement with the experimental observations, and the slip crack was inversely

S. Liang, Q. Dai, W. Huang, X. Wang
National Key Laboratory of Helicopter Aeromechanics
Nanjing University of Aeronautics and Astronautics
Nanjing 210016, China
E-mail: huangwei@nuaa.edu.cn

S. Liang, Q. Dai, W. Huang, X. Wang
College of Mechanical and Electrical Engineering
Nanjing University of Aeronautics and Astronautics
Nanjing 210016, China

X. Sun, D. She
AECC Hunan Aviation Powerplant Research Institute
Zhuzhou 412002, China

**ADVANCED
SCIENCE NEWS**

www.advancedsciencenews.com

**ADVANCED
ENGINEERING
MATERIALS**

www.aem-journal.com

proportional to the wear rate and independent of the contact geometry. Basseville et al.[17] investigated the relation between wear and crack initiation in TC4 alloy under fretting conditions using 2D FEA. Wear was observed to dominate at the beginning of the experiments in the absence of any cracks. Furthermore, 2D and 3D fretting wear simulations revealed that 3D models provided more accurate predictions compared with the experimental results.[19]

Several factors affect the service life of mechanical components undergoing fretting, including surface condition, contact configuration, normal load, and frequency. Many efforts have been devoted to exploring the effects of different surface engineering techniques, like shot peening,[24–26] rolling,[27] and solid lubrication coatings,[28,29] on the fretting behavior of titanium alloys. Huang et al.[26] applied femtosecond laser shock peening on TC4 alloy to create a submicron oxide layer and rough surface, which reduced the friction coefficient at the start of the fretting wear. Du et al.[29] observed a significant enhancement in the fretting wear and fatigue life of TC4 after depositing diamond-like carbon and graphite-like carbon films.

Surface textures, such as grooves or microdimples, have emerged as a viable means of improving the tribological performance of sliding surfaces.[30–34] Until now, the researchers have majorly focused on the investigation of the influence of surface texture on the fretting wear behavior of titanium alloys for the point contact condition, and punch/plane contact condition remains underexplored. The main mechanisms by which surface textures modulate fretting damage need more clarity. Moreover, the effect of the critical design parameters, such as texture depth, also needs better understanding. To address these issues, this study employs a finite element method (FEM) to investigate the effect of grooved surface texture on the fretting behavior of TC4 alloy having punch/plane contact configuration under both the PSR and the GSR.

2. FEM Model and Validation

2.1. Fretting Wear Model

The fretting wear model is based on the Archard and energy models.[35–37] The Archard model can be expressed by Equation (1)

$$\frac{V}{\delta} = K_W \cdot P \tag{1}$$

where V is the total wear volume, δ is the sliding distance, K_W is the Archard wear coefficient, and P is the normal load.

For the energy wear model, the wear energy dissipation between the contact interface is assumed to be proportional to the wear volume. Therefore, the energy model can be expressed by Equation (2)

$$V = K_{EW} \cdot E_D \tag{2}$$

where, K_{EW} is the energy wear coefficient obtained experimentally and E_D is the cumulative dissipated energy throughout the wear process, and it can be expressed by Equation (3)

$$E_D = \int Q d\delta = \int \mu P d\delta \tag{3}$$

where Q is the shear force and μ is the coefficient of friction (CoF).

The Archard model established a relationship between wear volume, normal load, and displacement amplitude, but it did not account for the variation of the CoF during fretting wear. While the energy wear model (based on the principle of energy conservation) incorporated the CoF. Therefore, the energy wear model was selected in this study to investigate the fretting wear of TC4 alloy under punch-to-plane contact conditions. CoF for TC4/TC4 alloy contact pair is 0.8[38,39] and the energy wear rate is 1.43e-5 m³ J⁻¹.[40]

The energy wear model was further refined to calculate the fretting wear volume. If A_E is the wear area, the wear depth h can be expressed by Equation (4)

$$h = \frac{V}{A_E} = \frac{K_{EW} \cdot E_D}{A_E} = \frac{K_{EW} \cdot \int \mu P d\delta}{A_E} \tag{4}$$

After differentiating and simplifying, we get

$$dh = \frac{K_{EW} \cdot Q}{A_E} \tag{5}$$

$$dh(x) = K_{EW} \cdot q(x) ds(x) \tag{6}$$

$$h(x) = \sum_i^n K_{EW} \cdot q(x)_i ds(x)_i \tag{7}$$

where $q(x)$ is the shear stress at x location and $h(x)$ is the wear depth.

The refined model can determine the depth of the worn surface at different locations, which helps to detect the variations in the worn surface profile.

2.2. Fatigue Prediction Model

The fatigue prediction model is based on the SWT equivalent stress[41] and a linear Miner's rule, which can predict the crack nucleation time. The SWT equivalent stress can be expressed by Equation (8)

$$\sigma_{SWT} = \left(E \cdot \sigma_{n,\max} \cdot \frac{\Delta \varepsilon_n}{2}\right)^{\frac{1}{2}} \tag{8}$$

where $\sigma_{n,\max}$ is the maximum eigenstress value on the critical plane during the cycle and $\Delta \varepsilon_n$ is the multiaxial strain amplitude on the critical plane (where the σ_{SWT} reaches its peak) during the cycle. It usually requires scanning across different angles in the polar coordinate system to locate this plane.[42]

The crack initiation life N_f can be acquired from Equation (9)

$$\sigma_{SWT} = (\sigma_f^2 \cdot N_f^{2\alpha} + E \cdot \sigma_f \cdot \varepsilon_f \cdot N_f^{\alpha+\beta})^{\frac{1}{2}} \tag{9}$$

where σ_f is the fatigue strength coefficient, ε_f is the fatigue ductile coefficient, α and β are the exponents, and E is the Young's modulus.

A linear Miner's rule can be used to accumulate the damage. For one cycle, the damage factor is equal to the inverse of the

Table 1. SWT constants for TC4 alloy.[43,44]

	σ_f	α	ε_f	β
1 mm crack	2030	−0.104	0.841	−0.688
10 μm crack	1817.2	−0.0978	8.841	−0.688

crack initiation life in this cycle, $1/N_f^{cycle}$. Therefore, the resulting fatigue damage 1of a block of cycles will be N_{block}/N_f^{cycle}. After n block of cycles, the accumulated damage can be expressed by Equation (10)

$$D = \sum_{block=1}^{n} \Delta D^{block} = \sum_{block=1}^{n} \frac{N_{block}}{N_f^{cycle}} \qquad (10)$$

Crack nucleation occurs when D approaches the unit value i.e., 1.

Table 1 presents the fatigue strength and exponent (σ_f and α), the fatigue ductile coefficient and exponent (ε_f and β), for TC4 alloy as reported by Dowling[43] and Madge.[44] These parameters were determined from fatigue tests, and failure was defined as the initiation of a 1 mm and 10 μm crack. To find the crack initiation life at small scales, a constant of 10 μm crack was used in this study.

2.3. Numerical Simulation and Validation

Numerical simulations were conducted using standard FEA software; ABAQUS. Punch and plane were modeled as 3D deformable parts (shown in **Figure 1**). The punch had a length of 2 mm, a flat surface of 1 mm, and a curvature radius of 0.5 mm, while the planes (both smooth and textured) had equal lengths and widths of 3 mm. Grooves were modeled on the textured plane having the width and inter-spacing of 40 μm and 200 μm, respectively, while their depth varied as 10, 20, and 40 μm (represented as T-10, T-20, and T-40 μm). TC4 alloy was selected as the material for both the plane and punch, with Young's modulus of 120 GPa and Poisson's ratio of 0.30.

Initially, a normal load P was applied at the top of the punch and fixed boundary condition was applied to the plane. In the next step, a periodic cyclic displacement having an amplitude δ (perpendicular to the grooves for textured surfaces) was applied to the bottom and side nodes of the plane. The complete model was meshed into eight-node linear brick (C3D8) elements.[45] Fine mesh was applied at the interface of the punch and plane, with a size of 40 μm, while a coarse mesh was applied to the remaining geometry as shown in Figure 1. The meshed model consisted of 115 625 elements and 126 893 nodes for the smooth plane configuration. To ensure simulation reliability, a uniform mesh sizing strategy was implemented within the 60 μm-thick subsurface regions beneath the upper surfaces of various textured planes.

Figure 2 presents the flow chart for fatigue life and wear depth calculations. A user-defined UMESHMOTION subroutine was used to apply the combination of the Archard energy model and FEM.[46] SWT equivalent stress and linear Miner's rule were used to calculate the fretting fatigue life. After each increment, ABAQUS executed the UMESHMOTION subroutine to update the worn surface profile, using arbitrary Lagrangian–Eulerian adaptive meshing technology. After completing the displacement cycle, the data, such as strain, stress, and coordinates, were exported. The maximum SWT stress value and its corresponding critical plane were determined by scanning the angle θ with respect to the Z-axis and the angle φ with respect to the Y-axis in polar coordinates. The crack initiation life N_f was calculated using Equation (10), and the Miner rule was applied to accumulate the damage factor.

The reliability of FEM was validated by comparing the contact pressure predicted by the FEM with the theoretical calculation (using the Ciavarella et al. expressions,[47,48] the schematic was shown in **Figure 3**), presented as Equations. (11–13)

$$\frac{PAR}{b^2} = \frac{\pi}{2} - \frac{a}{b}\sqrt{1 - \left(\frac{a}{b}\right)^2} - \sin^{-1}\left(\frac{a}{b}\right) \qquad (11)$$
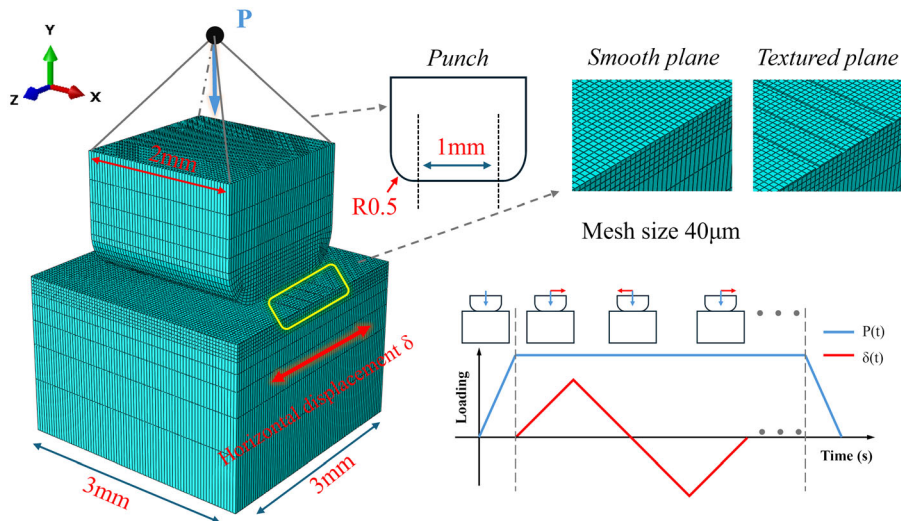

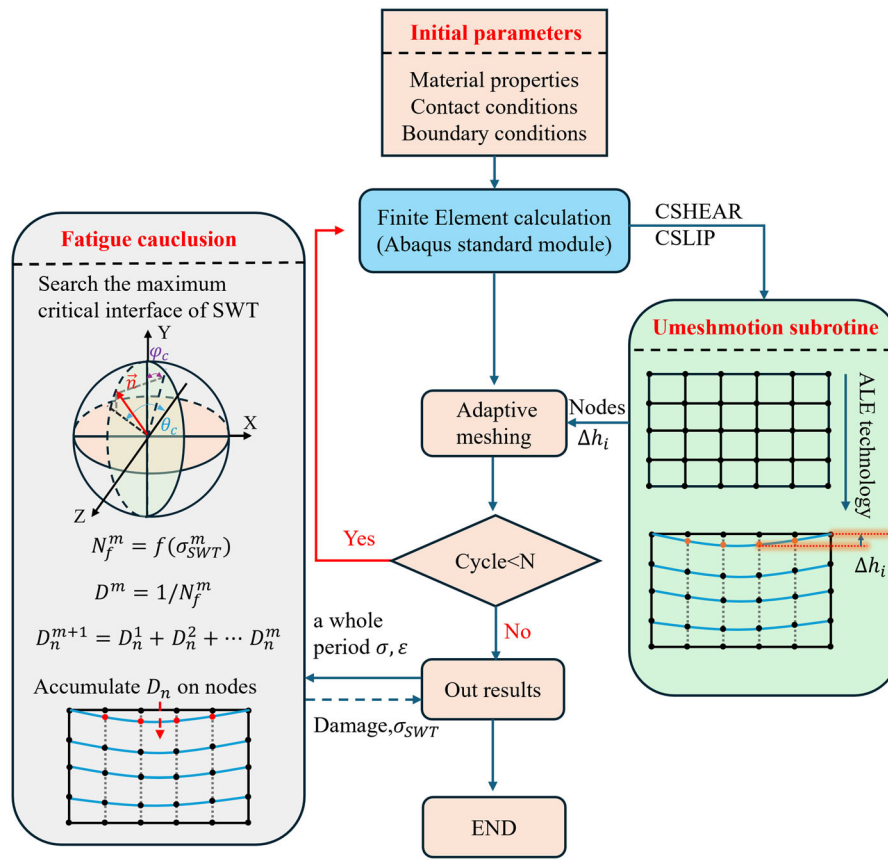**Figure 1.** The meshed model and boundary conditions for the fretting contact pair.

Figure 2. The flow chart demonstrates fatigue life and wear depth calculations.
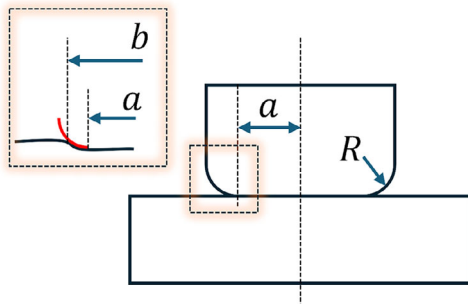

Figure 3. Schematic of the punch/plane contact.

$$A = 4*(1 - \nu^2)/E \qquad (12)$$

$$P(x) = -\frac{b}{AR}\left[1 - \frac{2}{\pi}\sin^{-1}\left(\frac{a}{b}\right)\right]\sqrt{1 - \left(\frac{x}{b}\right)^2} \qquad (13)$$

where R is the radius of the rounded corner; a is the semi-width of the punch flat; b is the semi-width of the contact region. P is the normal load; A is the composite elastic modulus; ν is the Poisson's ratio, and $P(x)$ is the pressure of the point(x).

Figure 4 presents the comparison of the contact pressure profiles calculated theoretically and using FEM.[47,48] The distribution patterns of the finite element results and theoretical
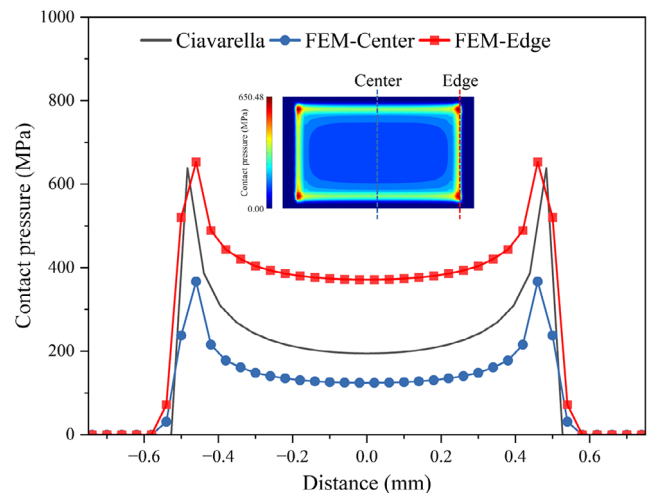

Figure 4. Comparison between theoretical and FEM solutions ($P = 400$ N, $\alpha = 1$ mm, and R $= 0.5$ mm).

calculations were similar, both demonstrated higher values at the edges and lower values at the center. The maximum values were nearly the same. In addition, the finite element results could present the difference in the contact pressures at the edges and at the center regions.
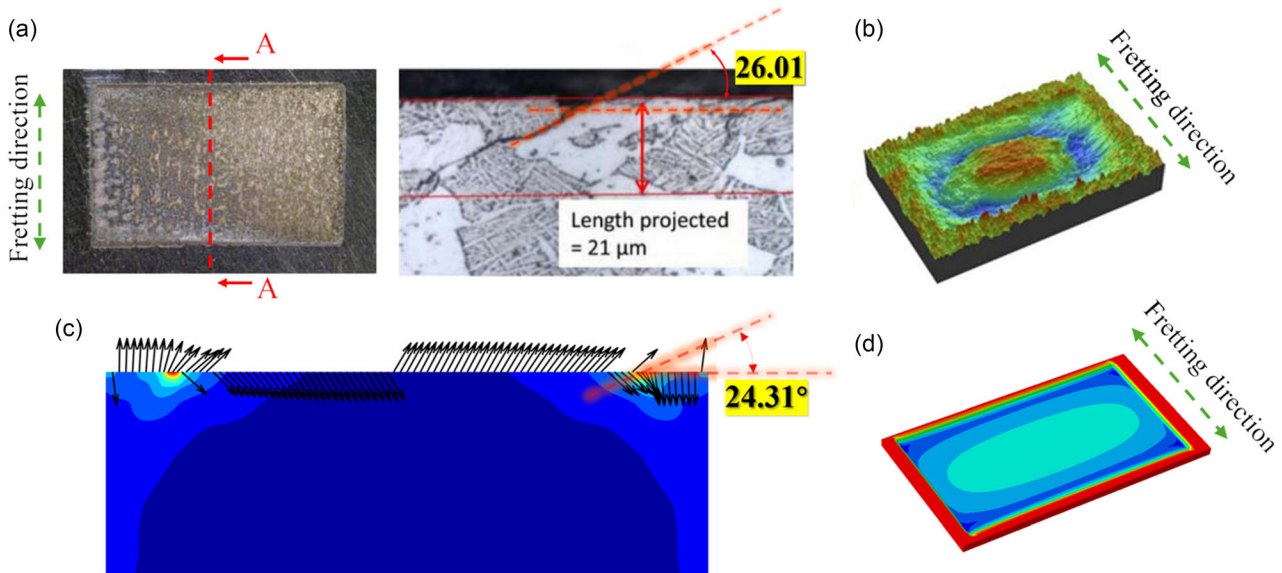
Figure 5. a) The cracks of punch/plane under PSR ($P = 5600$ N, $\delta = \pm 40\,\mu m$);[49] b) wear profile of punch/plane under GSR ($P = 4000$ N, $\delta = \pm 150\,\mu m$);[50] c) SWT stress distribution and the critical plane vector under PSR predicted by FEM; d) the wear profile under GSR predicted by FEM.

The finite element wear simulation results and fatigue calculations were also verified by comparing with the results of Refs. [49,50] **Figure 5a** presents the surface morphology of the titanium alloy after fretting tests under PSR. The wear was observed to be minimal within the contact area, whereas cracks emerged at the contact edges with an orientation angle of $\approx 26.01°$ to the surface.[49] Figure 5c presents the distribution of SWT equivalent stress on the cross section at the center of the contact area under the PSR. It was observed that the maximum SWT equivalent stress in this study also occurs at the edge, at an angle of $\approx 24.34°$ to the surface. This indicated that cracks were prone to form at the edges at a direction angle of 24.34° to the surface. When compared with the experimental results of Arnaud et al.[49] the error in the prediction of crack initiation angle was about 6.5%. Figure 5b presents the wear morphology from fretting tests under GSR,[50] and Figure 5d presents current simulation results. Due to the limitations of the FEM model, the accumulation of wear debris at the edges could not be accurately simulated. However, both the simulation and experimental results exhibited a similar trend, characterized by mild wear in the central region and severe wear at the edges and corners.

3. Results and Discussions

3.1. Effects on Contact and Kinetic Behavior

Figure 6 presents a comparison of contact pressure distributions in smooth and textured surfaces with varying groove depths (at $P = 400$ N). For the smooth surface, the maximum contact pressure of 650.48 MPa was obtained at the sample edges. For the textured surface, the maximum contact pressure of 737.07 MPa (T-10 μm) was observed, and the values gradually decreased with the increase in groove depth i.e., 668.84 MPa (T-40 μm). The maximum pressure concentration occurred near the contact edges for

both smooth and T-40 μm surfaces, while the T-10 μm and T-20 μm configurations showed peak pressures at the groove peripheries. It indicated that when the surface texture was shallow, the location of maximum contact pressure changed, and the increased contact pressures appeared at the edge of the grooves. The shallower the grooves, the higher the contact pressures.

Figure 7 presents a comparison of shear stress distribution for smooth and textured surfaces (at $P = 400$ N). The lower values were predicted at the center of the contact region, and the higher values at the edges of the contact region, similar to the contact pressure distribution. However, the maximum shear stress observed on the textured surface exhibited a significant increase compared to that on the smooth surface. In textured surfaces, the peak shear stress location shifted from the lateral boundaries of the contact region to the edges of the outermost texture. The introduction of surface textures not only elevated the shear stress magnitude at the contact interface but also redistributed stress concentrations, forming new shear stress peaks along both lateral boundaries of the textured region. Furthermore, an increase in groove depth was correlated with a reduction in shear stress magnitude on the textured surface, similar to the trend observed in contact pressure distribution.

It is known that the fretting regime primarily relies on the normal load and displacement amplitude.[51] **Figure 8** presents the tangential force–displacement curves for smooth and textured surfaces under the displacements of 5–10 μm with a fixed normal load ($P = 400$ N). According to the fretting map theory, the shape of the curves implies the fretting regime. The linear, parallelogram, and elliptical curves correspond to the PSR, the GSR, and the mixed slip regimes, respectively.[20] The tangential force and displacement curves for both smooth and textured surfaces were found to be similar, indicating that the textured surface did not change the kinetic behavior in the punch/plane fretting. At a displacement of 5 μm, all the curves displayed a linear shape,
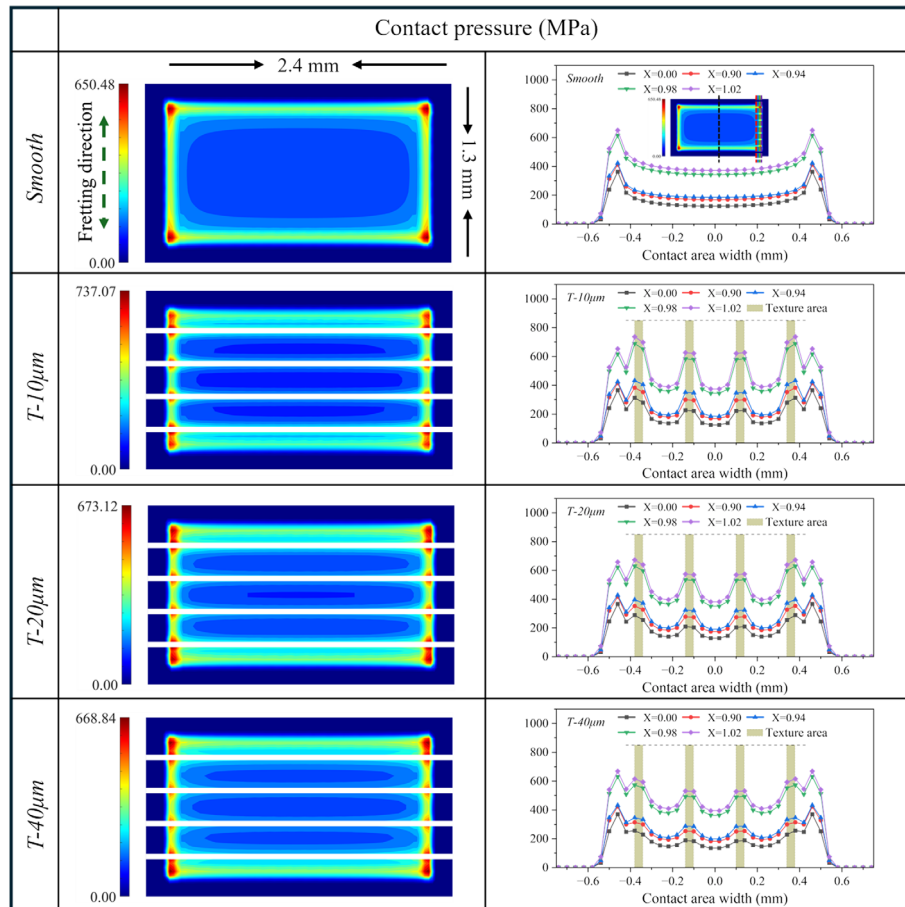
Figure 6. Comparison of the contact pressure in smooth and textured surfaces with varying groove depth.

indicating the PSR. At the displacement of 6 μm, a transition from a linear to an elliptical shape was observed, indicating the mixed slip regime. While further increasing the displacements to 7, 8, 9, and 10 μm, these curves transformed into a parallelogram shape, representing the GSR.

Figure 9 presents the tangential force–displacement curves for the smooth and the textured surfaces under variable normal loads and at a constant displacement of 10 μm. These curves exhibited similar patterns for both surface types. As the load increased from 100 to 1000 N, the curve profiles transitioned from parallelogram to linear shapes, indicating a shift from the GSR to the PSR. **Figure 10** presents the relative slip distribution and the ratio of shear stress to contact pressure at $P = 400$ N and $P = 1000$ N. The relative slip within the contact region decreases significantly with an increase in load. Since the local shear stress was insufficient to overcome the maximum static friction force, the ratio of shear stress to contact pressure was lower than the CoF, resulting in a sticking phenomenon throughout the contact area.

3.2. Effects on Fretting Wear

Figure 11 presents the wear morphology under the PSR ($P = 400$ N, Displacement $= 5$ μm). Both smooth and textured surfaces exhibited less wear depth, and the primary wear was located along the edges of the contact area parallel to the fretting direction. Since the higher shear stress was located at the edges of the contact area in PSR (as shown in Figure 7), most of the contact area remained in an adhesive state, resulting in less sliding and limited material wear. The maximum wear depth on the smooth and textured surface (T-10 μm) was about 0.21 μm, and it increased with the texture depth, reaching 0.23 μm for the T-40 μm. This trend corresponds to the variation in relative slip for the PSR, as shown in Figure 10. Additionally, the wear profile curves exhibited a slightly deeper wear on both sides of the grooves, which might be caused by the shear stress concentration at the edges.

Figure 12 presents the wear morphology in the contact area under the GSR ($P = 400$ N, Displacement $= 50$ μm). Unlike the PSR, significant relative sliding and severe wear were observed in the GSR. Consistent with the shear stress distribution as shown in Figure 7, excessive wear predominantly occurred at the edges rather than the center. The maximum wear depth of 4.22 μm was observed for the smooth surface, which was about a hundred times greater than that in the PSR. Since the shear stress on the textured surfaces was higher, the maximum wear depth for the textured surfaces was slightly higher than that of the smooth surface, i.e., 4.65 μm. Analogously, the

**ADVANCED
SCIENCE NEWS**

www.advancedsciencenews.com

**ADVANCED
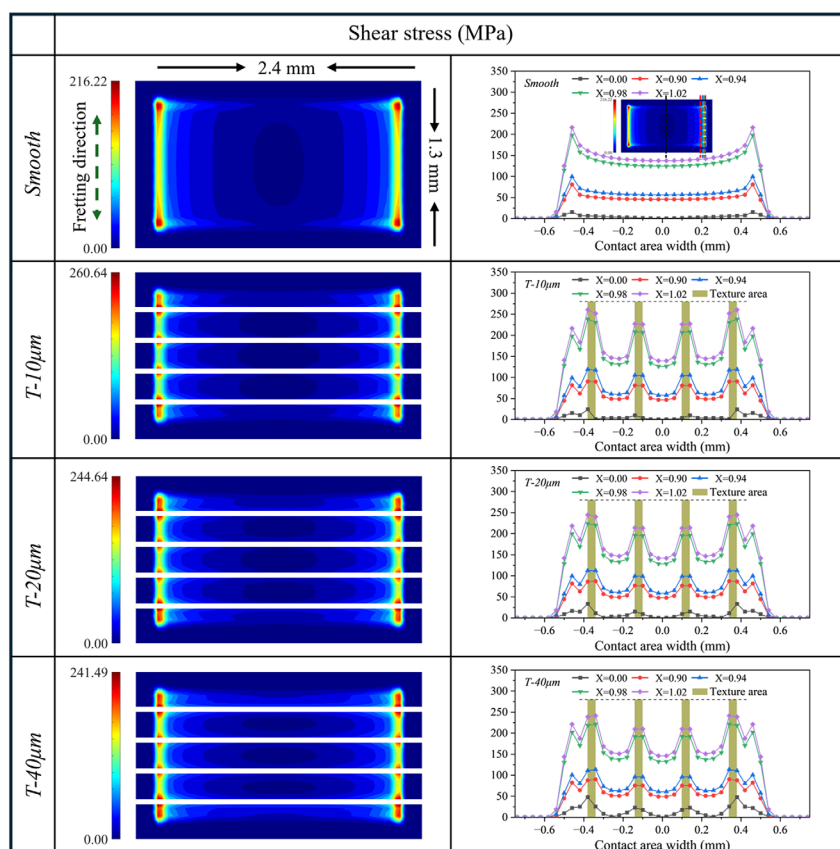ENGINEERING
MATERIALS**

www.aem-journal.com

Figure 7. Comparison of the shear stress for smooth and textured surfaces ($P = 400$ N).
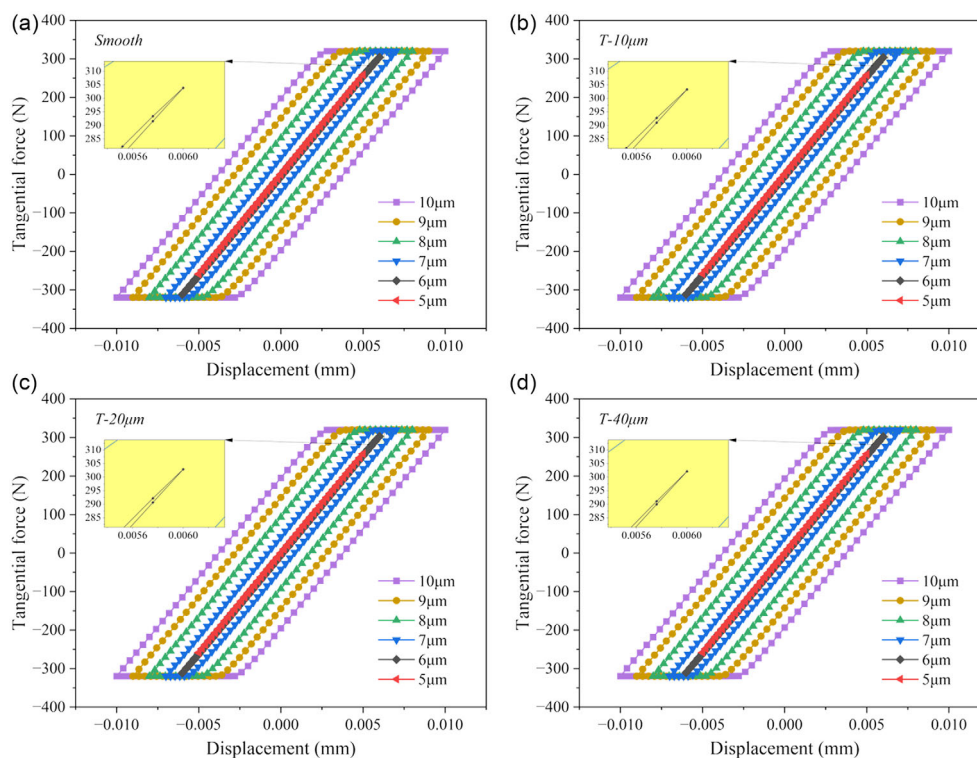

Figure 8. The tangential force–displacement curves for smooth and textured surfaces a) Smooth, b) T-10 μm, c) T-20 μm, d) T-40 μm.
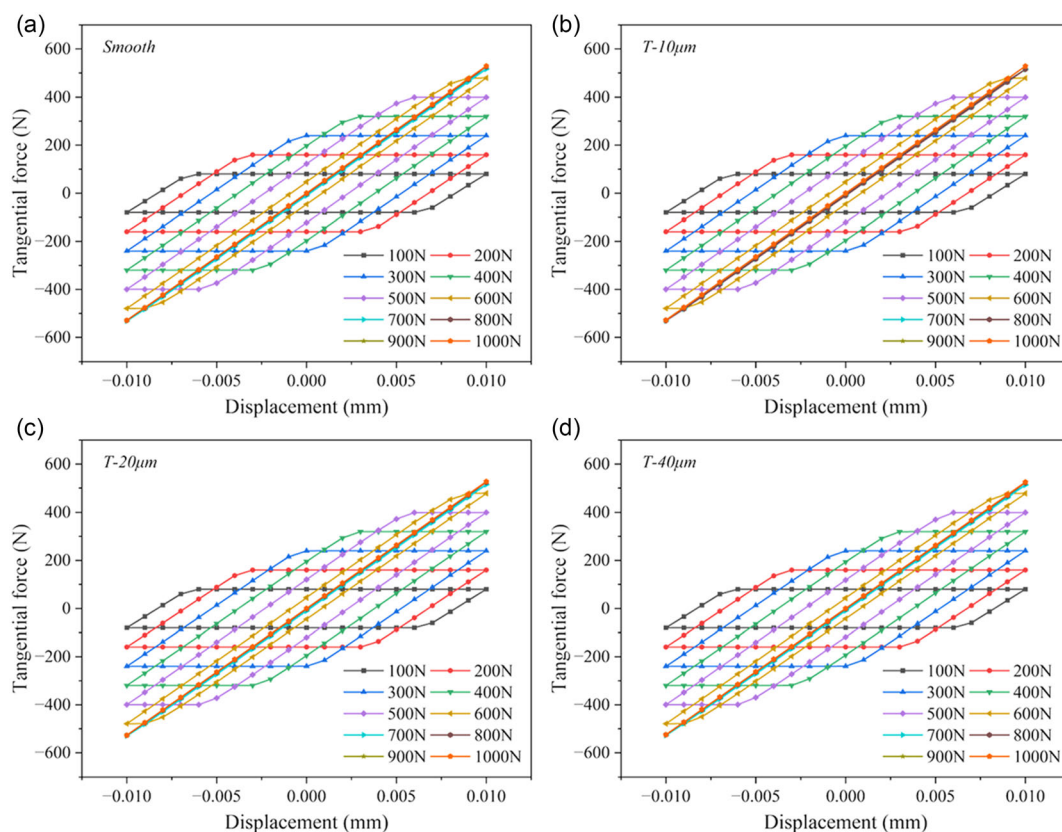
Figure 9. The tangential force–displacement curves for smooth and textured surfaces at varying loads and fixed displacement a) Smooth, b) T-10 μm, c) T-20 μm, d) T-40 μm.
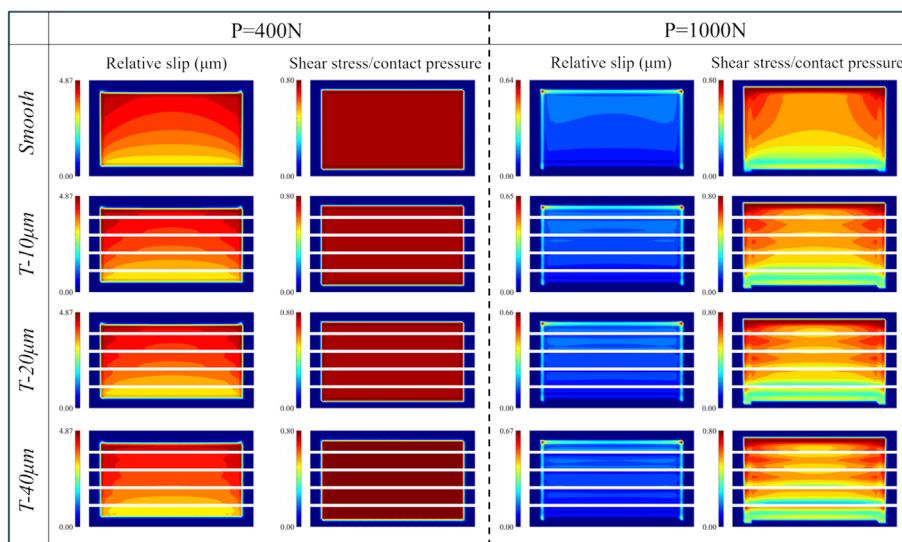

Figure 10. Comparison of the relative slip and the shear stress/contact pressure at fixed displacement.

wear depth on both sides of the texture was slightly greater than that in the adjacent regions according to the cross-sectional curves. However, this distinction was less obvious in the GSR due to excessive wear.

Figure 13a presents a comparison of wear volumes observed in the PSR (displacement = 5 μm) and in the GSR (displacement = 50 μm). About 100 times greater wear volume was observed in the GSR when compared with the PSR. Compared to the smooth
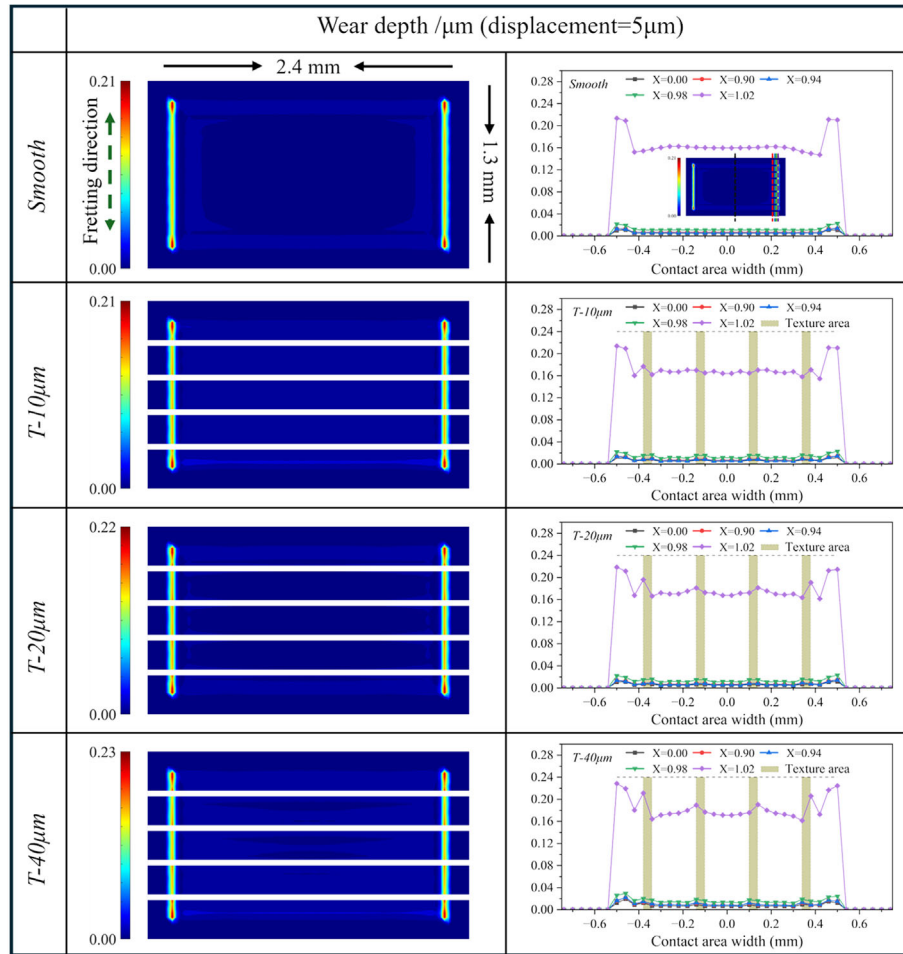
Figure 11. The wear morphology under the PSR ($P = 400$ N, $\delta = 5$ μm).

surface, the wear volume of the T-10 μm textured surface was decreased by about 0.53%, while T-20 and T-40 μm surfaces exhibited an increase of 0.92% and 0.49%, respectively. Hence, it can be concluded that the texture did not exacerbate material wear in the contact area at the displacement of 50 μm.

Figure 13b presents the wear volume and the maximum wear depth of various surfaces under different normal loads. Since the relative slip diminished with increasing normal load, the transition appeared from the GSR to the PSR. With an increase in loads, the maximum wear depth and wear volume of all surfaces were initially increased and then decreased. At a displacement of 10 μm, the wear volume of textured surfaces increased with the texture depth. Furthermore, the wear volumes of T-10 and T-20 μm textured surfaces (with shallower texture depths) were lower than that of the smooth surface. This result contrasts sharply with the wear behavior observed at a displacement of 50 μm, indicating that the effect of texture on wear varies under different slip distance conditions.

Therefore, Figure 13c illustrates the wear volume and maximum wear depth of various surfaces under the same normal load but with different displacements. Both the maximum wear depth and wear volume were increased with the displacement.

At smaller displacements (≤ 30 μm), there was no significant difference in maximum wear depth between smooth and textured surfaces. However, as the displacement exceeded 30 μm, a significant increase in the maximum wear depth of textured surfaces was observed, with the disparity between textured and smooth surfaces. Due to the smaller contact area of textured surfaces compared to smooth surfaces, the wear volume of textured surfaces remained similar to that of the smooth surfaces.

3.3. Effects on Fretting Fatigue

Figure 14 presents the distribution of equivalent SWT stress for both smooth and textured surfaces at the 1000th cycle. The distribution patterns of equivalent SWT stress were similar for both surfaces, exhibiting lower stress in the central region and higher stress at the ends of the fretting displacement path, with peaks primarily located at the corners. The equivalent SWT stress under the PSR was lower than that under the GSR. However, as discussed in Section 3.2, the wear under the GSR was more severe than that under the PSR, and the material wear rate exceeded the rates of crack initiation and growth. Although the equivalent SWT stress was higher in the GSR, the risk of
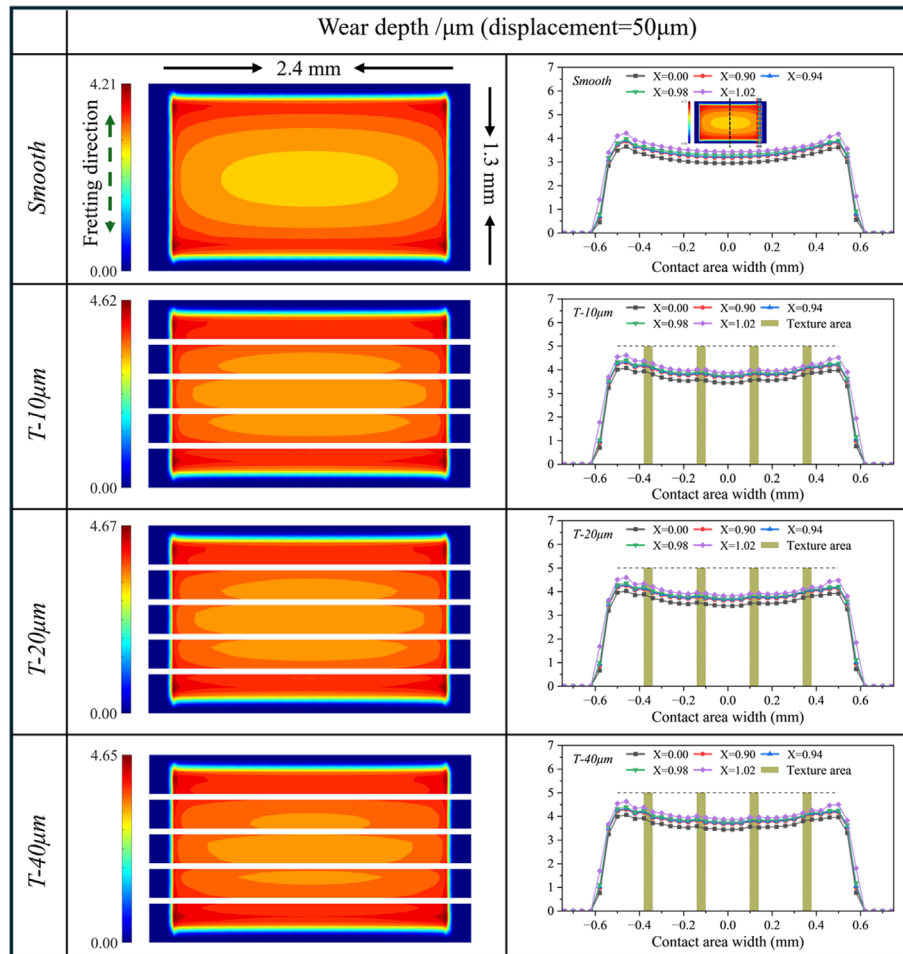
Figure 12. The wear morphology under the GSR ($P = 400$ N, Displacement $= 50$ μm).

fatigue crack initiation is greater in the contact region under PSR. These results are in agreement with the Basseville's and Arnaud's findings.[17,49] Due to this fact, aerospace engine applications frequently employ wear-resistant coatings to suppress fretting fatigue cracks at interfacial surfaces.

For the textured surfaces, the discontinuity introduced by the texture increased the stress-strain levels during fretting conditions. As a result, the equivalent SWT stress increased with the texture depth, leading to a shorter crack initiation life and making fatigue crack nucleation more obvious. **Figure 15** demonstrates the distribution of equivalent SWT stress and the orientation of critical plane normal vectors on the YZ cross section at the location of maximum equivalent SWT stress identified in Figure 14. Unlike the smooth plane, where the equivalent SWT stress was uniformly distributed across the contact interface, the textured surface exhibits stress concentration at the edges of the texture. This indicates that the textured surface also has a risk of crack initiation at the edges, particularly at the outer side. Although the maximum equivalent SWT stress was higher on the textured surface, the orientation of the critical plane normal vector at the location of maximum stress remained the same. Hence, surface texturing does not alter the direction of potential fatigue crack initiation under the PSR.

Figure 16 illustrates the cumulative damage factor for each surface after 10 000 fretting cycles under the PSR and the evolution of equivalent SWT stress along with the damage factor during the process. In terms of the cumulative damage factor, the smooth surface exhibited the lowest value of 0.798 after 10 000 fretting cycles. The cumulative damage factors for the textured surfaces were slightly higher than the smooth surfaces and increased with texture depth. For T-40 μm, it reached a value of 0.849 after 10 000 fretting cycles. It indicates that the textured surface T-40 μm has a shorter crack initiation life under the PSR, and its fatigue life was reduced by ≈6.3%, with a higher risk of crack initiation compared to smooth surfaces. Additionally, the risk of crack initiation increased with increasing groove depth.

The evolution of equivalent SWT stress exhibited a slight decrease with increasing cycles for all surfaces. This may be attributed to the minor wear during fretting, which alters the stress–strain state at the interface. Additionally, the evolution of cumulative damage factors exhibited a difference between smooth and textured surfaces. For the smooth surfaces, the risk of crack initiation was mainly concentrated at the ends of the
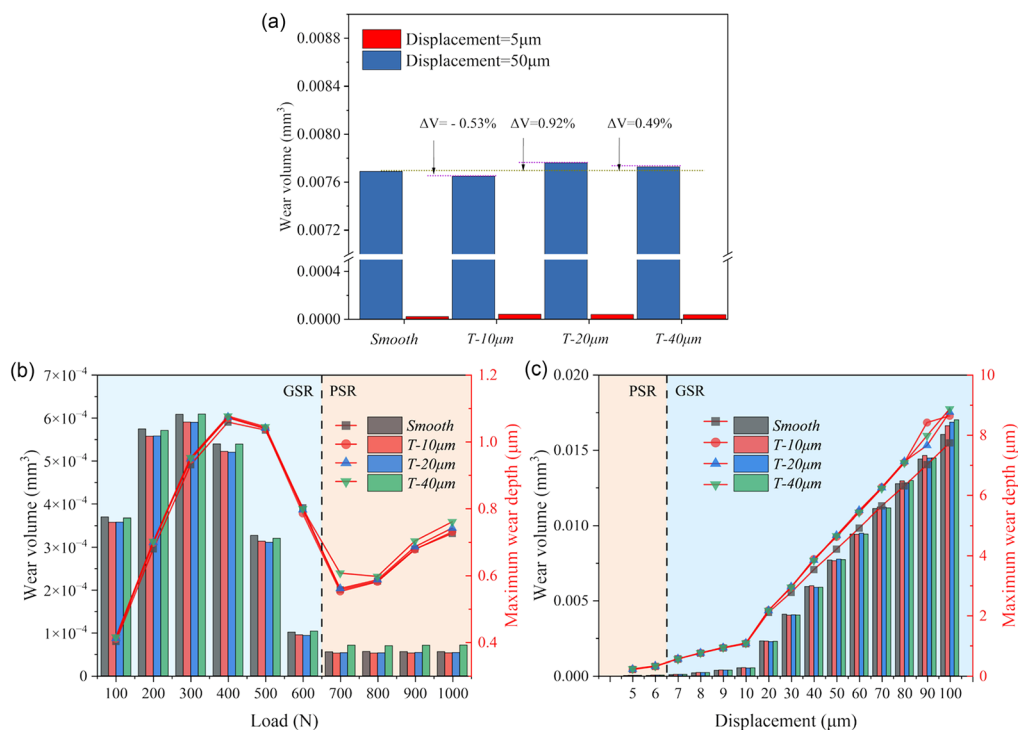
Figure 13. a) Wear volume at different surface conditions, b) wear volume and maximum wear depth at different normal loads (displacement = 10 μm), and c) wear volume and maximum wear depth at different displacements (Normal load = 400 N).
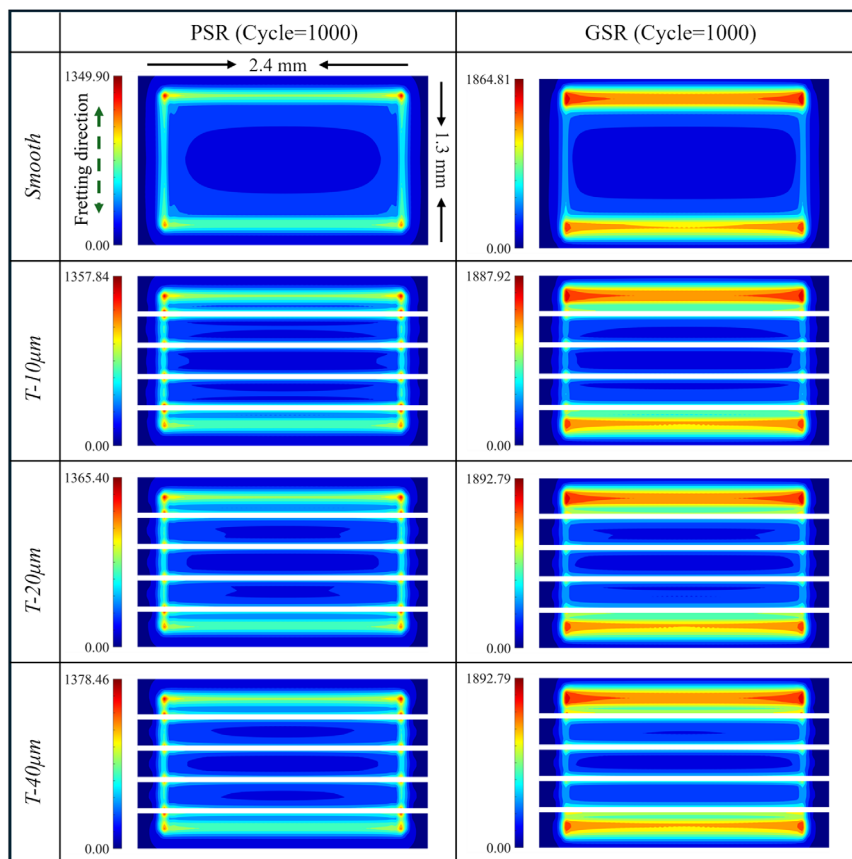

Figure 14. Distribution of equivalent SWT stress for different surfaces under the PSR and the GSR conditions.
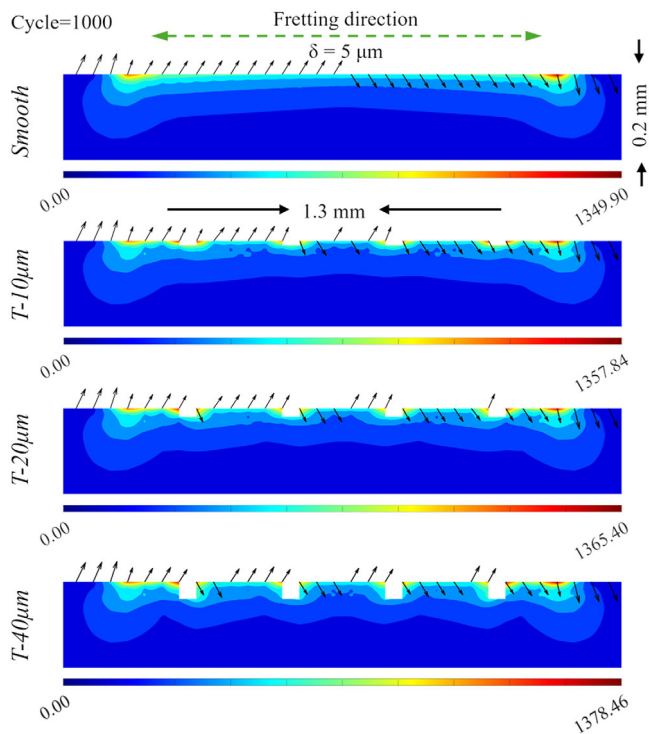
**ADVANCED
SCIENCE NEWS**

www.advancedsciencenews.com

**ADVANCED
ENGINEERING
MATERIALS**

www.aem-journal.com

Figure 15. The cross section at the maximum equivalent SWT stress for different surfaces ($P = 400$ N, $\delta = 5$ μm).

contact area. In contrast, textured surfaces exhibited higher equivalent SWT stress levels on both sides of the texture, leading to increased cumulative damage factors and a greater risk of crack initiation. This was particularly evident for textures with shallower depths (T-10 μm). When the texture depth was insufficient, the location for the crack initiation shifted from the edge of the contact area to the outer side of the grooves near the edge. This phenomenon was related to the alteration of shear stress distribution at the contact interface caused by the texture. As mentioned above, when the texture was too shallow, shear stress peaks moved from the edge to the outer side of the grooves.

4. Conclusions

In this work, the Archard energy wear model was applied to simulate the fretting wear behavior of smooth and textured (different texture depths) TC4 alloy planes under the punch/plane contact. The SWT model was used to calculate the fatigue damage, and the linear Miner rule was used to accumulate it to evaluate the fatigue crack risk in different planes. The following conclusions can be drawn from this research work: 1) The presence of surface texture does not significantly alter the kinetic behavior at the interface under punch/plane contact conditions. The fretting states (PSR or GSR) of smooth and textured surfaces are nearly identical under the same loading conditions; 2) In the PSR, both smooth and textured surfaces exhibited less wear, with damage primarily manifesting as crack initiation caused by fretting. With
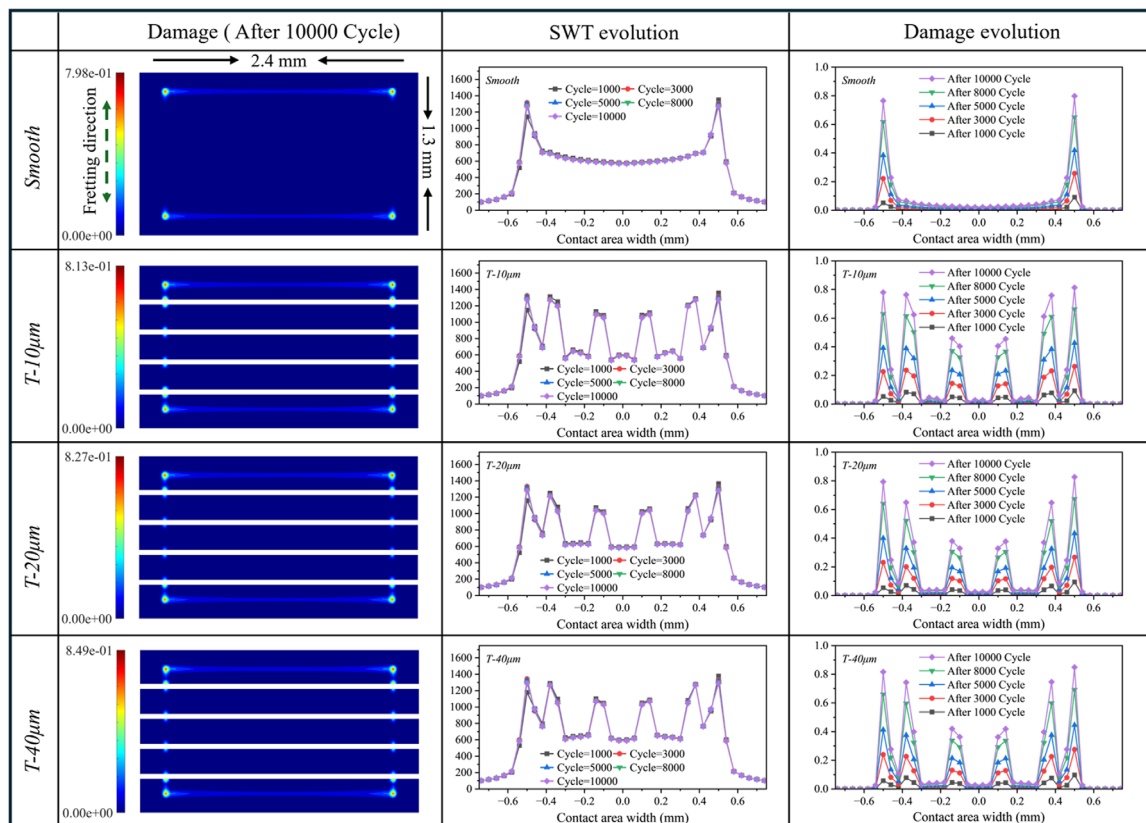

Figure 16. The damage factor after 10 000 cycles and the evolution of SWT and damage during the fretting ($P = 400$ N, $\delta = 5$ μm).

an increase in texture depth, the crack initiation life was decreased with a maximum reduction of ≈6.3%; 3) In the GSR, both smooth and textured surfaces exhibited similar wear patterns with mild wear at the central region and severe at the edges. Such a result is consistent with the distribution of the shear stress; 4) For the textured surfaces (at displacements ≤30 μm), the maximum wear depth was similar to that of smooth surfaces, and the wear volume was slightly lower. However, at larger displacements, the maximum wear depth and the wear volume of textured surfaces exceeded those of the smooth surface.

Conflict of Interest

The authors declare no conflict of interest.

Author Contributions

Shenglin Liang: data curation (lead); software (lead); writing—original draft (lead). **Xuanqi Sun**: conceptualization (lead). **Dingjun She**: visualization (lead). **Qingwen Dai**: investigation (lead). **Wei Huang**: writing—review editing (lead). **Xiaolei Wang**: supervision (lead).

Data Availability Statement

The data that support the findings of this study are available from the corresponding author upon reasonable request.

[1] S. A. Brown, C. A. C. Flemming, J. S. Kawalec, H. E. Placko, C. Vassaux, K. Merritt, J. H. Payer, M. J. Kraay, *J. Appl. Biomater.* **1995**, *6*, 19.

[2] R. D. Mindlin, H. Deresiewicz, *J. Appl. Mech.* **1953**, *20*, 327.

[3] X. Bian, C. Wei, Y. Liu, C. Wei, *Eng. Failure Anal.* **2024**, *157*, 107875.

[4] J. Zhang, J. Peng, B. Li, J. He, J. Liu, X. Xu, M. Zhu, *Proc. Inst. Mech. Eng. Part J.: J. Eng. Tribol.* **2024**, *239*, 59.

[5] Y. Yuan, G. Zhao, X. Zhao, L. Qian, S. Ma, F. Wang, *Tribol Int.* **2024**, *193*, 109407.

[6] B. Van Peteghem, S. Fouvry, J. Petit, *Wear* **2011**, *271*, 1535.

[7] F. T. Zhang, Y. L. Liang, Y. Z. Wu, C. Yin, J. Zhang, S. Yang, X. Huang, *Mater. Res. Express.* **2022**, *9*, 6513.

[8] Y. Ren, J. Cao, P. Tang, P. Yang, M. Li, Z. Li, J. Peng, H. Shen, X. Fan, M. Zhu, *Eng. Failure Anal.* **2024**, *166*, 108846.

[9] S. Fouvry, C. Paulin, S. Deyber, *Tribol Int.* **2009**, *42*, 461.

[10] M. L. Yang, J. L. Xu, J. Huang, L. W. Zhang, J. M. Luo, *J. Therm. Spray Technol.* **2024**, *33*, 2408.

[11] S. Fouvry, P. Arnaud, A. Mignot, P. Neubauer, *Tribol Int.* **2017**, *113*, 460.

[12] S. Fouvry, P. Duó, P. Perruchaut, *Wear* **2004**, *257*, 916.

[13] S. Fouvry, C. Paulin, T. Liskiewicz, *Tribol Int.* **2007**, *40*, 1428.

[14] C. H. Hager, J. H. Sanders, *Wear* **2004**, *257*, 167.

[15] J. A. Araújo D. Nowell, *Tribol Int.* **2009**, *42*, 1276.

[16] I. R. Mccoll, J. Ding, *Wear* **2004**, *256*, 1114.

[17] S. Basseville, G. Cailletaud, *Wear* **2015**, *328*, 443.

[18] P. Arnaud, S. Fouvry, S. Garcin, *Wear* **2017**, *376*, 1475.

[19] S. Basseville, D. Missoum-Benziane, G. Cailletaud, *Comput. Mech.* **2019**, *64*, 663.

[20] M. X. Cai, P. Zhang, Q. W. Xiong, Z. Cai, S. Luo, L. Gu, L. Zeng, *Tribol Int.* **2023**, *177*, 107930.

[21] S. Xu, X. Jing, P. Zhu, H. Jin, K.-W. Paik, P. He, S. Zhang, *Mater. Charact.* **2023**, *206*, 113389.

[22] R. Ji, Y. Liu, Y. Zhang, F. Wang, *Int. J. Refract. Met. Hard Mater.* **2011**, *29*, 117.

[23] L. Wang, G. Xiang, Y. Han, T. Yang, G. Zhou, J. Wang, *Int. J. Mech. Sci.* **2025**, *286*, 109887.

[24] V. Fridrici, S. Fouvry, P. Kapsa, *Wear* **2001**, *250*, 642.

[25] J. Vázquez, C. Navarro, J. Domínguez, *Int. J. Fatigue* **2012**, *40*, 143.

[26] X. Huang, K. Chen, L. Zhou, R. L. Narayan, U. Ramamurty, *Surf. Coat. Technol.* **2024**, *494*, 131353.

[27] Z. H. Wang, Y. H. Lu, H. Y. Zhang, T. Shoji, *Tribol Trans.* **2016**, *59*, 923.

[28] V. Fridrici, S. Fouvry, P. Kapsa, *Surf. Coat. Technol.* **2003**, *163*, 429.

[29] D. Du, D. Liu, Z. Ye, X. Zhang, F. Li, Z. Zhou, L. Yu, *Appl Surf Sci.* **2014**, *313*, 462.

[30] W. Huang, L. Jiang, C. Zhou, X. Wang, *Tribol Int.* **2012**, *52*, 87.

[31] A. Rosenkranz, P. G. Grützmacher, C. Gachot, H. L. Costa, *Adv. Eng. Mater.* **2019**, *21*, 1900194.

[32] X. Wang, W. Liu, F. Zhou, D. Zhu, *Tribol Int.* **2009**, *42*, 1118.

[33] S. Yuan, W. Huang, X. Wang, *Tribol Int.* **2011**, *44*, 1047.

[34] R. Ji, Q. Zhao, L. Zhao, Y. Liu, H. Jin, L. Wang, L. Wu, Z. Xu *Tribol. Int.* **2023**, *180*, 108218.

[35] S. Pan, C. Li, T. Jia, Y. Wang, *Wear* **2024**, *550–551*, 205405.

[36] J. F. Archard, *J. Appl. Phys.* **1953**, *24*, 981.

[37] S. Fouvry, P. Kapsa, L. Vincent, *Wear* **1996**, *200*, 186.

[38] O. Jin, S. Mall, *Wear* **2004**, *256*, 671.

[39] V. Sabelkin, S. Mall, *Strain* **2006**, *42*, 11.

[40] S. Garcin, S. Fouvry, S. Heredia, *Wear* **2015**, *330*, 145.

[41] K. Smith, *J. Mater.* **1970**, *5*, 767.

[42] H. Proudhon, S. Fouvry, G. Yantio, *Int. J. Fatigue* **2006**, *28*, 707.

[43] N. E. Dowling, *Fracture, And Fatigue*, 4th ed., Pearson, Boston **2013**.

[44] J. Madge, S. Leen, P. Shipway, *Int. J. Fatigue* **2008**, *30*, 1509.

[45] Z. Wang, H. Zhang, Z. Li, G. Li, J. Zhang, J. Zhang, H. Hassan, Y. Yan, A. Hartmaier, T. Sun, *Wear* **2019**, *430–431*, 1007.

[46] A. Cruzado, M. A. Urchegui, X. Gómez, *Wear* **2012**, *289*, 26.

[47] M. Ciavarella, D. A. Hills, G. Monno, *Proc. Inst. Mech. Eng. Part C: J. Mech. Eng. Sci.* **1998**, *212*, 319.

[48] M. Ciavarella, G. Macina, G. P. Demelio, *J. Strain Anal. Eng. Des.* **2002**, *37*, 493.

[49] P. Arnaud, S. Fouvry, S. Garcin, *Tribol Int.* **2017**, *108*, 32.

[50] C. Mary, S. Fouvry, J. M. Martin, B. Bonnet, *Wear* **2011**, *272*, 18.

[51] J. Li, Y.H. Lu, *Wear* **2013**, *304*, 223.